CONF-9311103--62

Note: This is a preprint of a paper submitted for publication. Contents of this paper should not be quoted or referred to without permission of the author(s).

For publication in *Determining Nanoscale Physical Properties of Materials by Microscopy and Spectroscopy*,
ed. by M. Sarikaya, M. Isaacson, and H. K. Wickramasighe,
Materials Research Society, Pittsburgh, Pennsylvania,
Fall Meeting of the Materials Research Society, Boston, Massachusetts,
November 29–December 3, 1993

# INCOHERENT IMAGING BY Z-CONTRAST STEM: TOWARDS 1 Å RESOLUTION

S. J. Pennycook, D. E. Jesson, and A. J. McGibbon

Solid State Division
Oak Ridge National Laboratory
Oak Ridge, Tennessee 37831-6030



SOLID STATE DIVISION
OAK RIDGE NATIONAL LABORATORY
Managed by
MARTIN MARIETTA ENERGY SYSTEMS, INC.
under
Contract No. DE-AC05-84OR21400
with the
U.S. DEPARTMENT OF ENERGY
Oak Ridge, Tennessee

December 1993

# INCOHERENT IMAGING BY Z-CONTRAST STEM: TOWARDS 1Å RESOLUTION

S. J. PENNYCOOK, D. E. JESSON, AND A. J. MCGIBBON
Solid State Division, Oak Ridge National Laboratory, Oak Ridge, Tennessee 37831-6030

## ABSTRACT:

By averaging phase correlations between scattered electrons a high angle detector in the scanning transmission electron microscope (STEM) can provide an incoherent, Z-contrast image at atomic resolution. Phase coherence is effectively destroyed through a combination of detector geometry (transverse incoherence) and phonon scattering (longitudinal incoherence). Besides having a higher intrinsic resolution, incoherent imaging offers the possibility of robust reconstruction to higher resolutions, provided that some lower frequency information is present in the image. This should have value for complex materials and regions of complex atomic arrangements such as grain boundaries. Direct resolution of the GaAs sublattice with a 300kV is demonstrated.

## INTRODUCTION

Figure 1 compares contrast transfer functions for coherent and incoherent imaging conditions under the same electron optical parameters, specifically a 300 kV accelerating voltage and an objective lens of 1mm $C_S$. The Scherzer resolution condition [1] in each case is marked, and it can be seen that the incoherent mode has a higher intrinsic resolution, given by 0.43 $C_s^{1/4}$ $\lambda^{3/4}$ compared to 0.66 $C_s^{1/4}$ $\lambda^{3/4}$ for the phase contrast case. More importantly perhaps, even beyond the Scherzer limit the incoherent transfer function shows no contrast reversals, so that it is always possible to identify the atomic sites directly by inspection of the image. In a region such as a grain boundary, atomic column separations are often significantly altered from those in the bulk. With coherent imaging this can result in the contrast of a column being reversed from that of an identical column in the bulk, so that image interpretation must necessarily rely on simulations of atomic structures derived for example from coincidence site lattice models. With incoherent imaging, if columns become closer together at the boundary they will simply merge together into one bright feature of elongated shape. They will still be identifiable by eye as two atomic columns, and in principle the resolution function could be deconvoluted from the image to extract atomic positions from such features. Since we can invert an incoherent image directly we are therefore no longer restricted to working from model structures. We have effectively bypassed the phase problem of electron diffraction and also avoided the problems of non-linear and non-local imaging associated with phase contrast methods.

Below we first show how the high angle detector destroys long-range phase correlations allowing us to consider each atom as scattering independently with a cross section that is close to the Rutherford value. This leads to an object function description of the imaging process, in which dynamical diffraction and anomalous absorption effects can be included in a straightforward manner. Finally, preliminary results from a 300 kV STEM are presented showing the direct resolution of the GaAs sublattice.

## PHONON-MEDIATED DESTRUCTION OF COHERENCE

It was realized very early that because the annular detector covers an angular range much larger than the separation between diffraction discs, interference effects in the transverse plane are effectively averaged, leading to images of single atoms and clusters that do not reverse contrast and show the resolution expected from the probe intensity profile [2-6]. For low inner

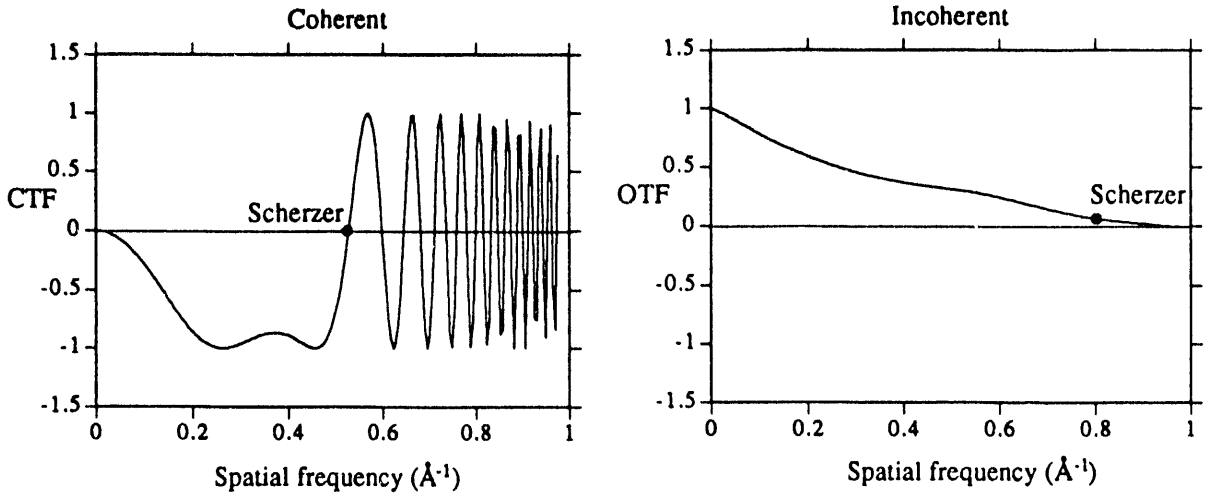


Fig. 1. Comparison of coherent and incoherent contrast transfer functions for a 300 kV microscope with 1mm $C_S$.

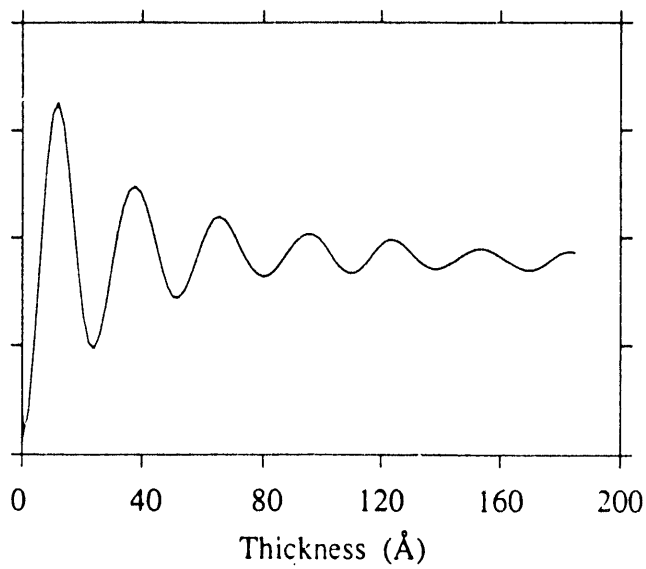


Fig. 2. The intensity of zero-layer coherent scattering reaching a 50-150 mrad annular detector shows an oscillatory thickness behavior. Calculated on a kinematic model for a 100 kV probe of 10.3 mrad semiangle located over a dumbbell in Si {110}.

detector angles, some residual transverse coherence effects remain [7]. This led to the widespread misconception that to achieve incoherent imaging *all* the scattered radiation had to be detected, so that at high resolution incoherent imaging would break down because of the so-called "hole in the detector" problem [8]. However, incoherent imaging of thin specimens can be achieved at atomic resolution simply by increasing the inner angle of the detector so as to collect a constant *fraction* of the total scattered radiation. [9]

Interference effects between atoms separated along the beam direction cannot however be destroyed by the geometry of the detector alone, as shown strikingly by Fig. 2. From a thin crystal, the intensity of zero layer coherent scattering increases initially as $n^2$, where n is the number of atoms along the column, but destructive interference rapidly sets in resulting in strong intensity oscillations, the intensity never rising above that scattered by a very thin slab [9]. It is this long range destructive interference that is destroyed by thermal vibrations, and leads to a thickness dependence that in the absence of dynamical effects and absorption would be linear. HOLZ diffraction also has a linear thickness dependence, and this has led to suggestions that the Z-contrast image might represent a HOLZ image [10,11]. However, it is easy to determine experimentally if the HOLZ contribution is significant, and for Si at room temperature it was found to be of the order of 1% of the total diffuse scattering detected [12]. Calculated HOLZ intensities are shown in Fig. 3, for three different Debye-Waller factors [13].

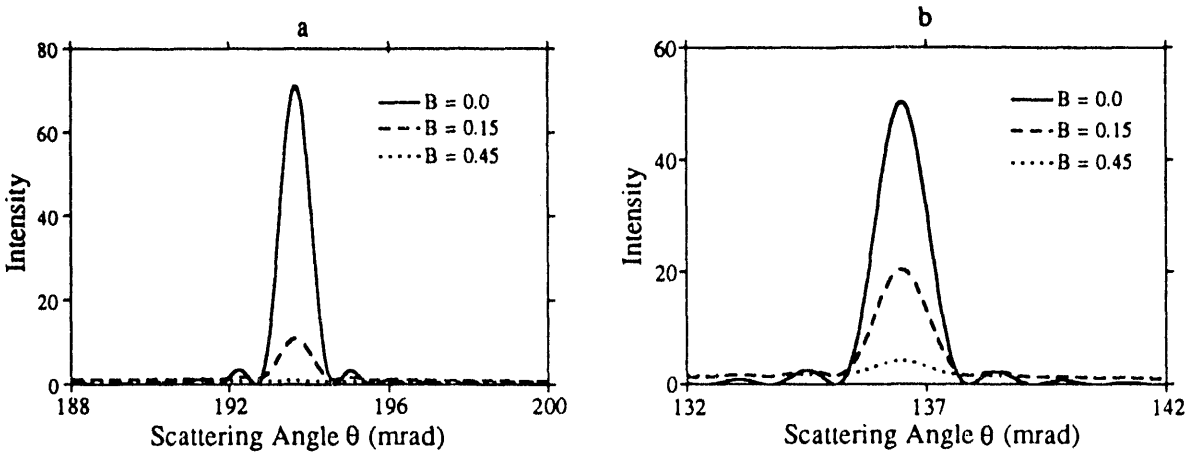


Fig. 3. Comparison of HOLZ ring intensities, azimuthally integrated, for stationary atoms with B = 0 (solid line), atoms at absolute zero, B = 0.15 (dashed line) and atoms at room temperature, B = 0.45 (dotted line). The atoms are spaced (a) 2 Å and (b) 4 Å apart along a column of length 200 Å.

B = 0 corresponds to stationary atoms, and predicts very strong HOLZ diffraction. However it is important to realize that stationary atoms are non-physical; even at absolute zero atoms are vibrating significantly due to zero point energy, and the curves with B = 0.15 represent the appropriate Debye-Waller factor for Si at absolute zero. Now to obtain a strong HOLZ image would require a thin annular detector centered on the HOLZ ring; for typical annular detector angles the HOLZ contribution is still only ~10%. Note that a HOLZ image could be very different from a diffuse scattering image, since it is sensitive to the atomic arrangement along the string, whereas the diffuse image is much less sensitive. At room temperature the HOLZ peaks are dramatically reduced.

Thermal diffuse scattering is normally described in terms of the Einstein model [14-16], in which atoms are treated as independently vibrating oscillators as indicated schematicallly in Fig. 4. This is a mathematically convenient but rather drastic representation of the effect of phonons. It means that each atom is treated as a separate independent source of thermal diffuse

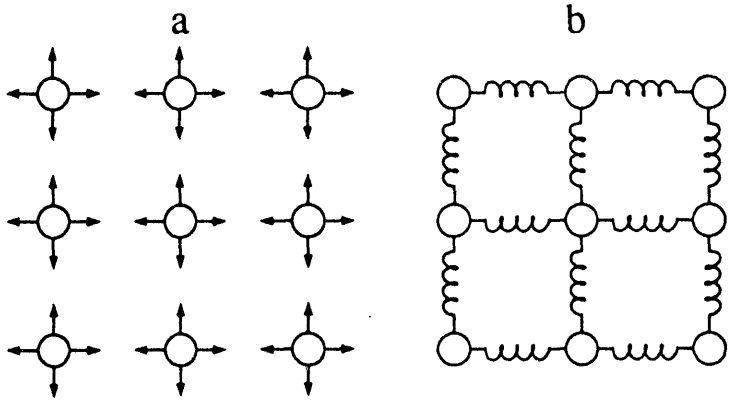


Fig. 4. Schematic comparing the (a) Einstein (or early Debye) model with (b) a phonon model of correlated vibrations

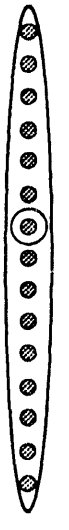

Fig. 5. Schematic comparing the correlation lengths of the coherent and diffuse components on an Einstein model of thermal vibrations.

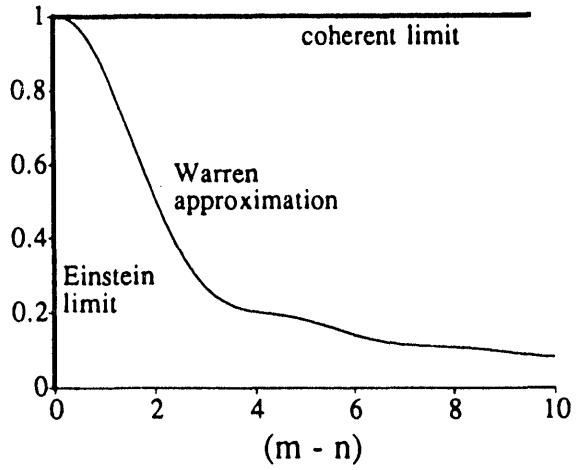


Fig. 6. Degree of coherence between an atom m spacings away from one at the origin, in the coherent scattering limit, the Einstein limit, and in the Warren approximation.

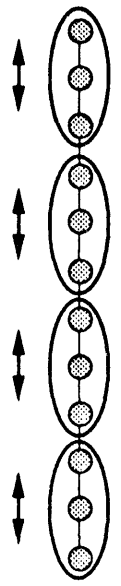

Fig. 7. Schematic showing a column scattering as n independently vibrating packets of atoms.

scattering, completely uncorrelated with any other atom in the crystal. The convenience of this approach arises from the fact that the scattering from a crystal splits into two components, one of which is completely coherent (a coherence volume comprising the entire sample), the other, the diffuse component, which is perfectly incoherent (the coherence volume around an atom contains only that atom) , as indicated in the schematic of Fig. 5. The ratio between the two is controlled by the Debye-Waller factor. In order to examine the degree of incoherence in the thermal diffuse scattering, it has been suggested that a weighted average of the coherence volumes can be used [17]. However, it is clearly preferable to go beyond the Einstein model in which total incoherence is assumed. A convenient model of thermal diffuse scattering including all orders of phonon scattering has been given by Warren [18] for the x-ray case, and recently developed for electron diffraction [13]. The most important result of this analysis is that it quantitatively describes the degree of coherence between atoms different distances apart in a column, as shown in Fig. 6. Changing scattering angle or Debye-Waller factor the correlation envelope changes smoothly from full coherence (horizontal line at unity) towards the Einstein model (a $\delta$-function at the origin). For the angles generally used for Z-contrast imaging, partial coherence remains between near neighbor atoms.

The physical interpretation suggested by this analysis is that a column of n atoms can be considered as n independently vibrating packets of atoms, as shown in Fig. 7. If the column is shorter than the packet size then coherent scattering dominates, (low angles and/or very short columns), but if the column is much longer than a packet then the column scatters incoherently, but with an atomic scattering cross section that is increased or decreased over the Einstein value depending on the phase of the residual correlations within the packet. For example, for columns greater than ~20Å in length and a detector inner angle of 75 mrad, an Einstein model will underestimate the scattering from a column of atoms 1Å apart by 25%, but overestimate the scattering from a column of atoms 2Å apart by 15%. It is worth noting however that these changes in cross section will only be noticeable if they are different for different columns, ie. if columns have different atomic spacings along the beam direction, otherwise these effects will just scale the overall image intensity.

## *s*-STATE PROBE PROPAGATION

Now that we have established that an incoherent scattering description is valid for high angles, we must next determine the illumination of each atom, which is controlled by the dynamical diffraction of the incoming probe. It has been noted previously that a STEM probe propagating along a low index zone axis tends to form narrow spikes around each atomic column having the envelope of the incident probe profile [19,20]. The reason for this is the special nature of the STEM illumination, a coherent probe having a rather large angular spread. Tightly bound *s*-type Bloch states add constructively as we integrate over this large angular range to construct the focussed probe, whereas other less localized states interfere destructively. The result is a great reduction in beam broadening and for a small enough incident probe we can achieve column-by-column illumination. This tendency is further enhanced for scattering processes that are *localized* at the atomic cores, high angle diffuse scattering or inelastic scattering with large energy losses, which preferentially selects these localized *s* type states. Dynamical diffraction manifests simply as a columnar channeling effect, and the image intensity can be written as a simple convolution with an object function peaked at each atomic site [12,21]. The object functions contains to first order the effects of dynamical diffraction and absorption, and predicts thickness behavior that agrees with experiment (Fig. 8.) The *s* states themselves are highly localized around each atomic column, with a diameter less than that of the incident probe, even for a 300 kV STEM. Closely spaced identical columns lead to molecular orbital like Bloch states, but under most conditions, the *s* states are insensitive to the nature and distribution of surrounding atoms. The object function is highly localized because only the intensity of the s-state is involved, not its emergent phase, (see Fig. 9). No supercell calculations are necessary, in fact, with complex materials or interfaces small model unit cells may be used to determine columnar channelling effects and an object function constructed in a column-by-column manner [21]. In thin specimens, the dominant contribution to the intensity of a column is always its composition; we have never found a situation in which the heavier columns are not the brightest in the image, although due to the higher absoption of the heavy strings the contrast does decrease with increasing specimen thickness. In very thick crystals there is no longer a high resolution image. Eventually, the intensity detected from the heavy material must become less than that detected from a lighter material, as multiple scattering sends electrons outside the range of the annular detector.

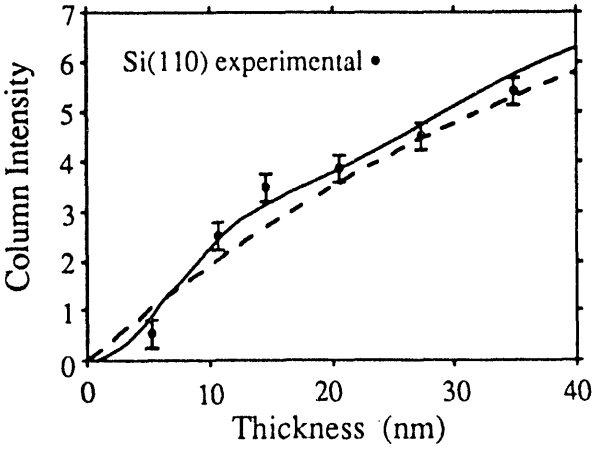


Fig. 8. Thickness dependence of image intensity from Si {110} on the *s*-state model (dashed line), and using all states (solid line), compared to experimental measurements (points).

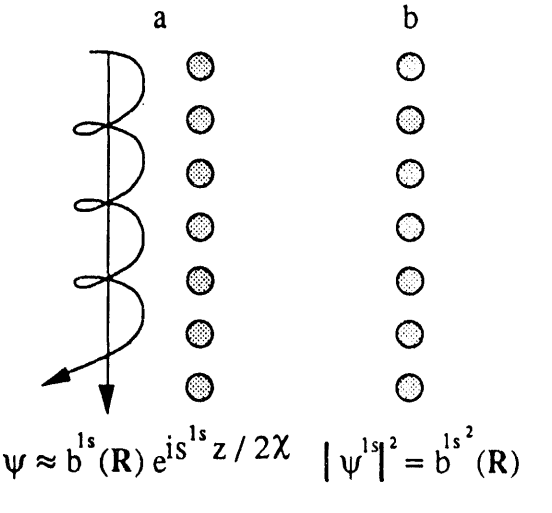


Fig. 9. (a) Coherent imaging measures the phase of the emergent s-state which is sensitive to tails of potentials from surrounding strings. (b) Incoherent imaging measures *s*-state intensity which is more local.

Incoherent imaging in perfect crystals is well explained in this picture, but a defect such as a dislocation that destroys the continuity of a column, through its associated strain fields, will alter the channeling effect of columns in the vicinity. Dislocations induce transitions to and from other Bloch states and can appear dark or bright depending on their depth in the sample and the inner-detector angle (22,23). Even end-on dislocations can induce strain fields that can bend nearby columns because of surface relaxation. The strain fields extend several atomic spacings, but within the strained region the positions of the heaviest columns can still be picked by inspection to an accuracy much better than one spacing, but further study of the effect of strain fields on the image is needed to extract dislocation core structures accurately.

## MAXIMUM ENTROPY IMAGE ANALYSIS

Incoherent imaging not only allows an intuitive first order structure determination, it also opens up the possibility of quantitiative and robust image analysis and reconstructions via maximum entropy methods [24,25]. Although it has been suggested that higher resolutions can be achieved through higher defocus values [26], the use of a non-Scherzer probe results in non-intuitive imaging and a return to a dependence on structure models, thus negating one of the key advantages of incoherent imaging. Figure 10. shows probe profiles and simulated images for Si {110} as a range of defocus, and although increasing the defocus from the Scherzer optimum probe increases the resolution from 1.25Å to 1.0Å at a defocus of 700Å, a strong subsidiary maximum appears around the central sharp peak resulting in a loss of image contrast and interpretability. A more robust approach is to use the optimum Scherzer probe and reconstruct the higher resolution information by maximum entropy. A probe near optimum is readily found experimentally by focussing for maximum contrast in the image.

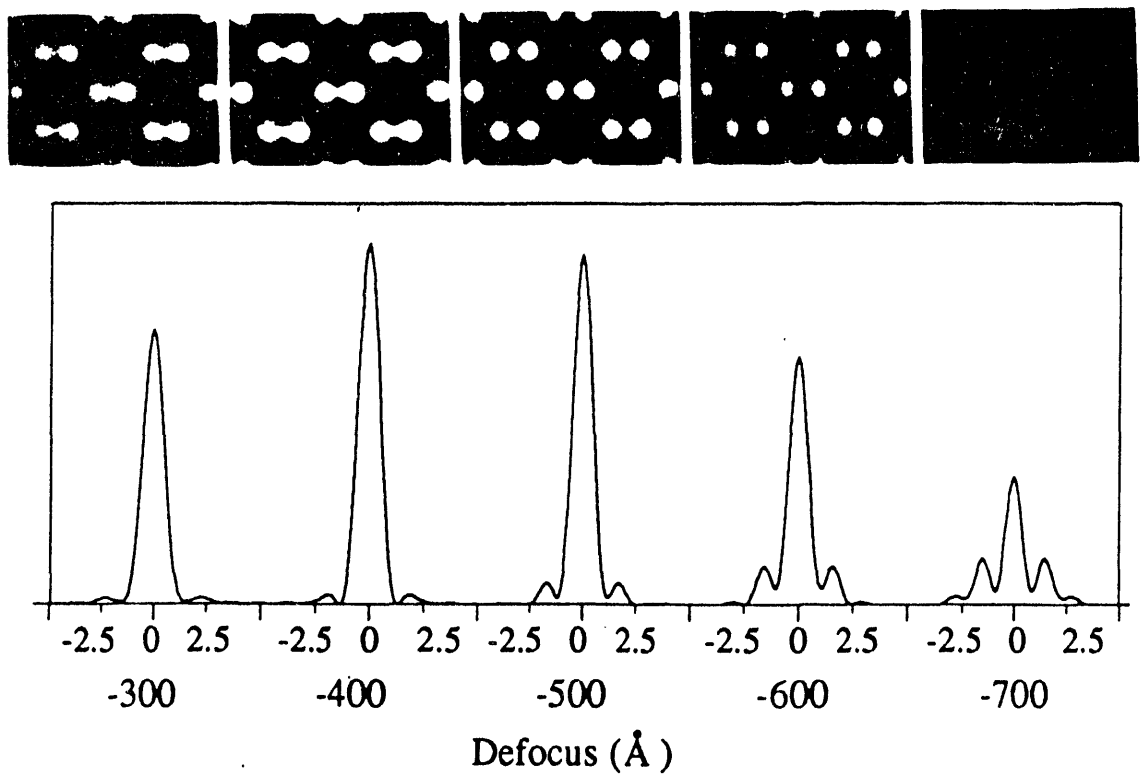


Fig. 10. Simulated focal series for Si {110} with corresponding probe intensity profiles, calculated for a 300 kV STEM with 1mm $C_S$ and a 9.3 mrad objective semiangle.

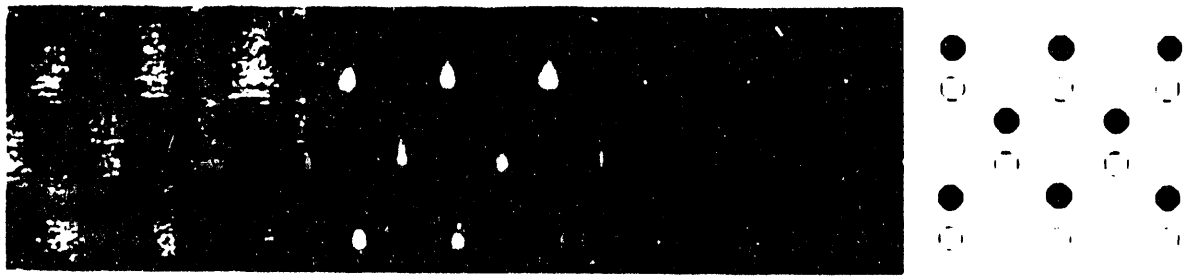

a b c d

Fig. 11. (a) Z-contrast image of GaAs showing direct resolution of the sublattice with a 300 kV STEM, with maximum entropy restorations for 25 (b), and 100 (c) iterations, compared to the projected structure (d).

As an example of this approach we show in Fig. 11. an image of GaAs [27] to which maximum entropy restoration has been applied. The reconstruction works from a point spread function defined by the user, in this case a Lorentzian with a FWHM of 1.3Å, and attempts to account for the experimental image intensity distribution by an array of point scatterers. This is clearly ideal for our situation, and depending on the number of iterations employed, the method can be used either as an efficient noise reduction technique or as a means of image quantification, providing positions and strengths of atomic columns together with individual error bars. 25 iterations produce significant sharpening of the image features (b) but 100 iterations are required to reduce the data to points (c). In all cases the polarity of the GaAs sublattice can be determined visually, even though the two columns are only two atomic numbers apart, and differ by only ~10% in their scattering power. The noise in the original image is translated into errors in position and intensity of the final points. From the region shown we find an intra-dumbbell separation of 1.46Å ± 0.16Å and an inter-dumbbell spacing of 1.37Å ± 0.21Å, which differ by less than 0.1Å from the correct (400) spacing of 1.41Å.

## FUTURE DIRECTIONS

The maximum entropy method offers an attractive means to quantify column positions and compositions at interfaces and grain boundaries, although further work is required to determine the best probe profiles to use. We have yet to try a realistic probe profile as shown in Fig. 10., and it would also seem attractive to attempt to extract the actual resolution function from a region of perfect crystal adjacent to an interface. This might allow the effects of astigmatism and residual crystal tilts to be corrected for by the reconstruction.

A second attractive direction is to utilize the probe channeling phenomenon and localised inelastic scattering events to obtain column-by-column spectroscopic information [28]. We have recently demonstrated a resolution of 2.7Å at a CoSi2/Si {111} interface using the Co-L edge [29]. With increasing accelerating voltage, although the range of the inelastic excitation increases, the probe size decrease at a faster rate and a resolution of 1.5Å at the Co-L edge is indicated for a 300 kV STEM. Combining Z-contrast imaging, maximum entropy analysis, and bonding information from parallel detection EELS offers much promise for the study of interface structure and chemistry.

## ACKNOWLEDGMENTS

The authors are grateful to S. L. Carney, J. T. Luck, and T. C. Estes for technical assistance. This research was sponsored by the Division of Materials Sciences, U.S. Department of Energy, under contract DE-AC05-84OR21400 with Martin Marietta Energy Systems, Inc.

## REFERENCES


1. O. Scherzer, J. Appl. Phys. **20** 20 (1949).
2. A. V. Crewe, J. Wall and J. Langmore, Science **168**, 1338 (1970).
3. A. Engel, J. W. Wiggins, and D. C. Woodruff, J. Appl. Phys. **45**, 2739 (1974).
4. A. V. Crewe, J. P. Langmore, and M. S. Isaacson, in Physical Aspects of Electron Microscopy and Microbeam Analysis, edited by B. M. Siegel and D. R. Beaman (Wiley and Sons, New York, 1975), p. 47.
5. J. Wall, J. Langmore, M. Isaacson, and A. V. Crewe, Proc. Nat. Acad. Sci. **71**, 1 (1974)
6. M. S. Isaacson, M. Ohtsuki, and M. Utlaut, in Introduction to Analytical Electron Microscopy, edited by J. J. Hren, J. I. Goldstein, and D. C. Joy, (Plenum Press, New York, 1979), p. 343 .
7. J. M. Cowley, Ultramicroscopy **2**, 3 (1976).
8. G. Ade, Optik **49**, 113 (1977).
9. D. E. Jesson and S. J. Pennycook, Proc. R. Soc. Lond.**A441**, 261 (1993).
10. J. C. H. Spence, J. M. Zuo, and J. Lynch, Ultramicroscopy **32**, 233 (1989).
11. R. F. Loane, P. Xu, and J. Silcox, Acta. Cryst. **A47**, 267 (1991).
12. S. J. Pennycook and D. E. Jesson, Ultramicroscopy **37**, 14 (1991).
13. D. E. Jesson and S. J. Pennycook, Proc. R. Soc. Lond. submitted (1993).
14. C. R. Hall and P. B. Hirsch, Proc. Roc. Soc. A **286**, 158-177 (1965).
15. D. M. Bird and Q A. King, Acta Cryst. **A46**, 202 (1990).
16. L. J. Allen and C. J. Rossouw, Phys. Rev. **B42**, 11644 (1990)
17. M. M. J. Treacy and J. M. Gibson, these proceedings.
18. B. E. Warren, X-Ray Diffraction, (Dover Publishing, New York, 1990).
19. J. Fertig and H. Rose, Optik **59**, 407 (1981).
20. R. F. Loane, E. J. Kirkland, and J. Silcox, Acta. Cryst. **A44**, 912 (1988).
21. S. J. Pennycook and D. E. Jesson, Acta Metall. Mater. **40**, Suppl. S149 (1992).
22. J. M. Cowley, and Y. Huang, Ultramicroscopy **40**, 171 (1992).
23. D. D. Perovic, A. Howie and C. J. Rossouw, Phil. Mag. Letts. **67**, 261 (1993)
24. S. F. Gull, and J. Skilling, IEE Proc. **131F** 646 (1984).
25. S. J. Pennycook, D. E. Jesson, M. F. Chisholm, A. G. Ferridge and M. J. Seddon, Proc. 10th Pfefferkorn Conf. on Signal and Image Processing, Cambridge, U. K. (Scanning Microscopy International, AMF O'Hare, in press).
26. P. Xu, E. J. Kirkland, J. Silcox, and R. Keyse, Ultramicroscopy **32**, 93 (1990).
27. A. J. McGibbon, S. J. Pennycook and Z. Wasilewski in Growth Processing and Characterization of Semiconductor Heterostructures, edited by G. Gumbs, S. Luryi, B. Weiss, and G. W. Wicks (Mater. Res. Soc. Proc. **326**, Pittsburg, PA, 1994, in press)
28. N. D. Browning, and S. J. Pennycook, Microbeam Analysis **2**, 81 (1993).
29. N. D. Browning, M. F. Chisholm, and S. J. Pennycook, Nature **366**, 143 (1993).

# END

DATE
FILMED
3/17/94